Incorporation and distribution of noble metal atoms in polyacrylonitrile colloidal particles using different polymerization strategies

*Anna Beltzung[1], Claudio Colombo[1], Maarten Nachtegaal[2], Hua Wu[1], Giuseppe Storti[1] and Massimo Morbidelli[1]**

[1]Department of Chemistry and Applied Biosciences, Institute for Chemical and Bioengineering, ETH Zurich, Switzerland

[2]Paul Scherrer Institute, 5232 Villigen, Switzerland

KEYWORDS: emulsion, nanoparticle, polymer, polyacrylonitrile, Palladium, Platinum, nanocomposite, hybrid material, single sites, STEM, EDX, XAFS

Abstract:

This work is focused on the incorporation of inorganic compounds into an organic framework. More precisely, noble metals are being incorporated *in-situ* in polyacrylonitrile colloidal particles (CPs) using, scalable and reproducible synthesis routes. For this purpose, oil-soluble platinum- and palladium-based precursors are used for physical entrapment based on mini-emulsion polymerization, while water soluble precursors of the same metals are used for the incorporation via chemical entrapment based on conventional emulsion polymerization. For the latter, it is shown that one can well alter the spatial distribution of the metal within the CPs by tuning the feeding strategy of the precursor. In addition, chemical entrapment requires the complexation of the metal with acrylonitrile, thus resulting in the incorporation of single atoms and dimers, as suggested by both X-ray absorption spectroscopy and indirectly by NMR-titration. The visualization of the extent of incorporation was performed by STEM-EDX on all synthesized CPs, while ICP-OES was applied for a quantitative evaluation. Finally, to prove the absence of large metal aggregates in the samples, high-resolution STEM was applied.

Introduction

Embedding valuable inorganic compounds, mainly metals or metal oxides, into a matrix has been intensively researched because modified and specific properties can be obtained in this way. These new functional materials are generally called doped materials or nanocomposites and exhibit a broad palette of possible combinations for various applications, such as biomass conversion [1], antibacterial purposes [2], cancer treatment [3, 4], optical and electrical properties[5] and tissue engineering[6].

Conventionally, metals or metal oxides are incorporated in silica, zeolites or metal organic frameworks (MOFs) for increasing the activity in catalytic applications or gas adsorption/storage purposes. In the case of zeolite, for example ZSM-5 was doped with precious metals (Ag, Cu, Ni, Pd, Ir and Ru) to successfully enhance the activity and selectivity of methanol conversion to hydrocarbons[7] while conventional Y-zeolite was ion-exchanged with TiO_2 as photocatalyst for the reduction of CO_2. [8] Intensive research has been carried out on the use of zeolites as sorbent or catalyst and, even though large-scale implementations exist, the need of cheaper materials with better mechanical and chemical resistances persists. [9] As for the MOFs, high H_2-storage was achieved by doping MOFs with Li^+ cations and replacing $Me_2NH_2^+$ from the framework. [10] More recent studies show the incorporation of gold-coated Pd nanoparticles and doxorubicin (chemotherapy medication) inside an acid degradable ZIF-8 MOF for chemo-photothermal treatment of cancer cells. [3] However, MOFs suffer from lack of thermal stability and exhibit high sensitivity towards water vapor and impurities. [11] Moreover, the use of expensive and toxic solvents for their synthesis hinders their large scale applicability. [12]

Besides the supports mentioned above, carbon-based materials represent a good alternative as matrices for metal incorporation. More specifically, polymers are becoming key for developing such composite materials due to their low cost, ease of synthesis and interesting properties such as viscoelasticity or versatility in composition. [13,14] In fact, thanks to the many available monomers, the choice of possible polymers is vast, and the same applies for the resulting nanocomposites. Additionally, the use of polymer can simplify the ability to pattern metallic nanoparticles by an in-situ cation reduction approach. [15,16] Those polymeric matrices find also applications in bioengineering, e.g. by embedding healing agents inside core-shell polymer microbeads, which could generate a very efficient and injectable self-healing

material. [17] There are also other forms of nanocomposite with polymeric matrix, for example vesicles with controllable size made from block copolymers (poly(acrylic acid-st)-b-poly(styrene)) are also used to incorporate Ag nanoparticle for catalytic purpose. [18] More importantly, in order to achieve major improvements in optic or electrical properties, the size and spatial distribution of the inorganic compound inside the polymer support have been carefully controlled. [19] In fact, even though the incorporation of microscale (10-100 nm) inorganic entities in bulk polymers (films, membrane, etc.) is already well explored [20–23], the incorporation of metallic nanoparticles inside polymer particles (with homogeneous or heterogeneous internal dispersion) is still being investigated. [24–26] Such dispersed materials are of interest in different cases, such as tracers for enhanced detection signal (optical sensing or detection in biological systems) or catalysis by impregnating cobalt on polyacrylonitrile particles. [27,28] Compared to single-component materials such as quantum dots (QDs), dyes or metallic nanoparticles, hybrid latex particles (i.e. inorganic nanoparticles dispersed inside colloidal polymer particles) overcome many disadvantages such as cytotoxicity resulting from metal ions leaching and colloidal stability issues (less aggregation than QDs in aqueous media). [29,30]

Incorporating nano-scaled inorganic entities, usually below 10 nm, in polymer colloids has gained an increased interest since this permits very remarkable improvements of the material properties, from thermal to mechanical [31–33] to the catalytic activity [34–36]. For example, the thermal resistance of coating was increased by embedding nanosilica particles of 7 nm in 150 nm copolymer particles made from methyl methacrylate, acrylic acid and butyl acrylate via batch emulsion polymerization [33]. Closer to this work, a hierarchical conductive polymer with enhanced properties was synthesized by incorporating homogeneously distributed 10 nm TiO_2 nanoparticles within poly-(styrene-divinyl-benzene-acrylonitrile) spheres. [5] The importance of the support was highlighted when incorporating well dispersed and stable 4-5 nm Pd nanoparticles inside mesoporous N-doped carbon made from the carbonization of melamine and glucose (with $ZnCl_2$ as porogen agent). [37] These authors report that N-doping is improving the immobilization and dispersion of Pd nanoparticles even after using the catalyst for a hydrogenation reaction. Based on the success of embedding nanoscale inorganic materials, efforts were made to introduce single atoms within the structure. Impregnating Pd on graphitic C_3N_4 led to mostly single metallic sites and showed increase in selectivity (nearly 100 % below 363 K and 2 bar)

and activity towards semi-hydrogenation reactions. [38] However, the synthesis of graphitic carbon nitride requires condensation at high temperature with release of ammonia and suffers a low yield and surface defects. [39]

Nevertheless, even though those aforementioned syntheses are promising in several fields, most of them stay complex (pre-treatment of inorganic entities or many synthetic steps [22,37,40]) and expensive (use of organic solvents and other reagents [36,41]) and result in low stability and efficiency, which is far from industrial needs [42,43]. Moreover, since the price of these metal-precursors is usually much higher than that of the support itself, the incorporation and spatial distribution need to be carefully designed, understood and assessed to avoid any waste. Accordingly, the full control of the distribution of these compounds within the support is necessary.

The most popular synthetic procedure for such hybrid materials is the so-called mini-emulsion polymerization. [44–46] In this process droplets containing monomer and inorganic entities are formed and the subsequent polymerization traps physically the inorganic nanoparticles inside the polymer particles. For example, the incorporation of 20-30 nm ceria nanoparticles inside polyacrylic particles was successfully performed with an approximate 1:1 relationship (1 CeO_2 nanoparticle in 1 polymer particle) via seeded mini-emulsion. [47] Since the scalability of mini-emulsion is non trivial given the high shear required in the droplet formation step, different synthetic routes are desirable, especially in view of large scale industrialization.

To address all these challenges (stability, simplicity of synthesis, costs etc.), colloidal particles (CPs) of polyacrylonitrile (PAN), a nitrogen-containing polymer suitable to incorporate metals and introducing porosity after pyrolysis, dispersed in water has been prepared by emulsion and mini-emulsion polymerization with incorporation of palladium and platinum precursors during the CP formation. This work reports the results of several synthetic techniques achieving different spatial distributions of atomic- or nanoscale Pt and Pd inside the PAN CPs. Such different spatial distributions and the strong embedding of the inorganic entities inside the polymer matrix enable the preparation of materials with promising properties and applications in catalysis or nanoplastic tracing (via metallic fingerprint) in the environment, e.g. in waste-water treatment plant and in agricultural soil.

1. Materials & methods

1.1 Materials

Acrylonitrile (Aldrich chemistry ≥ 99.0%), abbreviated AN, was employed as monomer. Oil soluble 2,2' Azobis(2-methylbutyronitrile), V67, and water-soluble potassium persulfate (KPS) from Merck (ACS, Reag. Ph. Eur) were employed as initiators. The initiator V67 was employed for mini-emulsion polymerization based on the recipe of Yang et al. 2015. [48] Potassium poly(ethylene glycol) 4-nonylphenyl 3-sulfopropylether (KPE) and sodium dodecyl sulfate (SDS) were used as surfactants. Hexadecane from Sigma Aldrich (99 % purity, Sigma Aldrich) was used as co-stabilizer in mini-emulsion. The oil-soluble metal-precursors used for the mini-emulsion incorporation were platinum(II) acetylacetonate ($Pt(acac)_2$) and palladium(II) acetylacetonate ($Pd(acac)_2$) both from Sigma Aldrich. Water-soluble precursors, K_2PdCl_4 and K_2PtCl_4, purchased from ABCR (99 %) and Aldrich (98 %), respectively, were used for emulsion polymerization. Deionized water was the reaction medium for all types of polymerization and was stripped with N_2 *(g)* prior to the start of the polymerization. All materials were used without further purification.

1.2 Synthesis of different latexes with incorporated noble metals

Two polymerization procedures were employed, namely, mini-emulsion and conventional emulsion polymerization.

Mini-emulsion is an oil-in-water type of emulsion and results in a physical entrapment of the inorganic molecules in the polymeric surrounding. [48] The experimental procedure involves high-shear treatment (usually by sonication) of a two-phase system comprising an aqueous phase, containing surfactants, and an oil-phase, containing the monomer, a co-stabilizer, an oil-soluble initiator and the metal precursor. The droplets originated from the latter phase entrap the metal-precursor, and the following polymerization step makes this entrapment much more effective, thus preventing any metal escape. The reaction was performed at 55 ˚C under stirring at 300 rpm. This procedure was mainly employed with the Pt-based oil-soluble metal precursor ($Pt(acac)_2$) since the use of the Pd-based precursor always

resulted in the formation of black solids, probably Pd(0), and very poor conversion. Accordingly, mini-emulsion procedures involving $Pd(acac)_2$ were not further considered in this work.

The sonication of the oil-in-water emulsion was performed using a Branson Ultrasonics Sonifier™ S-450 (Switzerland). In the case of PAN very intense sonication is required due to the monomer hydrophilicity. Hence, a series of several sonication periods of 2 min at 90 % was applied until the mini-emulsion droplets were stable over time. In order to increase the hydrophobicity of the droplets, a low-boiling organic solvent was added to the mini-emulsion, dichloromethane (DCM). The sonication was performed in an ice-water bath to avoid temperature increase that could anticipate the polymerization. The polymerizations performed in mini-emulsion and involving pure AN and $Pt(acac)_2$ will be indicated by the acronym MEPANPt and the corresponding recipe is described in Table 1.

Table 1. Recipe for mini-emulsion of Pt-containing PAN. The overall reaction mass was 60 g.

	Ingredient	*Weight %*
Water-phase	Water [a)]	85
	SDS [b)]	3
	KPE [b)]	3
Oil-phase	Monomer [a)]	15
	$Pt(acac)_2$ [b)]	1
	Hexadecane [b)]	5
	DCM [b)]	26.67 (3 mL)
	V67 [b)]	4

[a)]with respect to total mass, [b)]with respect to monomer

In conventional emulsion polymerization, water-soluble surfactants (SDS and KPE), initiator (KPS) and metal precursors (K_2PdCl_4 and K_2PtCl_4) were used. For all polymerizations, SDS was used for micellar nucleation, and the reactor was evacuated and filled with N_2 *(g)* 3 times until it was finally closed to avoid any radical deactivation due to the presence of O_2 *(g)*. In addition, all the synthesis involving AN required the use of an additional surfactant (KPE) to ensure good stability and prevent spontaneous aggregation of the nanoparticles inside the reactor. [49]

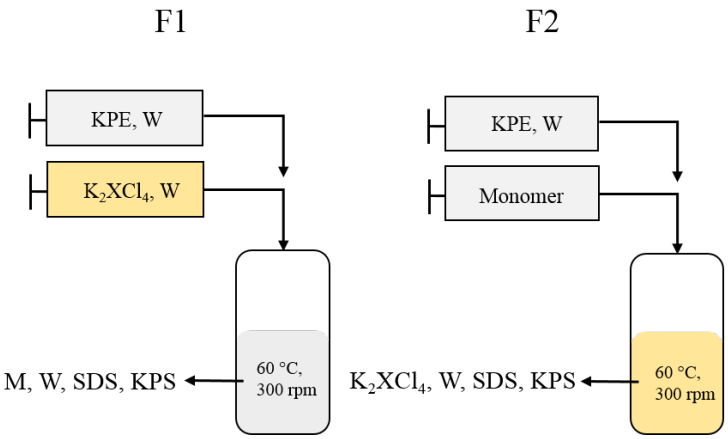

Fig. 1 - Schematic representation of the 2 types of conventional emulsion polymerization for the incorporation of noble metal in polymer nanoparticles. M = monomer, W = water, SDS = sodium dodecyl sulfate, KPE = Potassium poly(ethylene glycol) 4-nonylphenyl 3-sulfopropylether, KPS = potassium persulfate, X = Pd or Pt

Semibatch reactions were run, applying two different feed strategies, resulting in different metal distributions inside the polymeric CPs. In the first case, feed strategy F1, monomer, water, SDS and KPS were initially charged to the reaction vessel, while the steric surfactant, KPE, and the metal precursor were fed in two different ways, F1a and F1b. In the first case, the additions of metal precursor and KPE are carried out quickly (2 min) after the onset of some opacity in the reaction mixture, *i.e.* after the nucleation start. On the other hand, the addition time of the metal precursor was much longer in F1b (30 min), thus favoring a more distributed incorporation of the metal inside the polymer particles. About KPE, half of it was added at the start of nucleation, while the other half was added at the end of the 30 min precursor feed.

In the second case, feed strategy F2, metal precursor, surfactant and initiator were initially charged while the monomer was fed quickly (2 min). Similarly as for F1b, half of the KPE was fed at the start of the nucleation, while the other half was fed 30 minutes later. F2 emulsion polymerization was performed by targeting two different solid contents, SC: one with 4% and the other with 10%, named F2 A and F2 B, respectively.

In each case, the feeding procedure of KPE was chosen based on the destabilization effect of adding salts inside a colloidal dispersion, as it acts as stabilizer. The schematic representation of the two

different feed strategies (F1 and F2) is illustrated in Fig. 1. The latexes produced by emulsion polymerization were named PANPd and PANPt when using K_2PdCl_4 and K_2PtCl_4, respectively, and the recipes are described in Table 2.

Table 2. Recipe for emulsion polymerization of Pt- or Pd-containing PAN; the overall reaction mass was 60 g at 10 % SC for F1a, F1b and F2 B, 25 g mass synthesis at 4 % SC for F2 A.

F1a & b	*Ingredient*	*Weight %*	
Initial charge	Water [a)]	90	
	SDS [b)]	3	
	Acrylonitrile [a)]	10	
Additional compounds dissolved in water	KPS [b)]	3	
	K_2XCl_4 [b)]	1.5	
	KPE [b)]	2	
F2	*Ingredient*	*Weight % - A*	*Weight % - B*
Initial charge	Water [a)]	96	90
	SDS [b)]	3	3
	K_2XCl_4 [b)]	1.5	1.5
Additional compounds dissolved in water	KPS [b)]	3	3
	KPE [b)]	3	3
Other feed	Acrylonitrile [a)]	4	10

[a)] with respect to total mass, [b)]with respect to monomer

After weighting separately the desired amounts of KPS, K_2XCl_4 (X = Pd or Pt) and KPE, ~4 g of water were taken from the initially weighted degassed water and added to each compound to ensure complete dissolution. In all cases, the evolution of the conversion was followed by thermogravimetric analysis (Halogen Moisture Analyzer, Mettler Toledo, Switzerland) by heating the samples up to 120 °C in air and measuring the corresponding weight loss. Dynamic Light Scattering (DLS) using a Zetasizer Nano Z (Malvern, UK) under backscattering geometry (at angle 173°) was employed to follow the aggregation kinetics of the dissolved K_2PdCl_4 or K_2PtCl_4 in (0.1 μm) filtered deionized water in the temperature range of 20-60 ˚C. For each temperature, an equilibrium time of 120 seconds was employed and 3 measurements were subsequently performed. All the produced latexes were filtered with a paper-filter to remove all possible agglomerates. In addition, another type of material was produced by adding 1.5

wt % K_2PdCl_4 (with respect to monomer) diluted in water after the synthesis of metal-free PAN latex. The latter was produced using a recipe reported elsewhere.[49]

1.3 Characterization of the incorporated noble metals

To visualize the metal dispersion in the nanoparticles, Scanning Transmission Electron Microscopy and Energy-Dispersive X-ray spectroscopy (STEM-EDX) were performed on all materials. Images with 1024 × 1024 pixels were obtained using a FEI Talos F200X electron microscope equipped with a Super-X SDD detector at an acceleration voltage of 200 kV, a spot size of number 6 and using high angle annular dark field (HAADF) detector. EDX elemental maps (hypermaps) were acquired by scanning the probe for 10 minutes at an energy of 40 keV to assess the K, M and L lines of palladium and 20 keV for the L and M lines of platinum. The combination of the two methods, i.e. STEM and EDX, allows imaging of the distribution of the metal atoms in the colloidal particles. The CP dispersions were diluted and a droplet was placed on a TEM-grid (lacey carbon film 300 mesh, Lucerna-Chem, Switzerland), which was put in an oven at 40 °C for drying.

To identify small noble metal nanoparticles (< 1 nm), High-Resolution STEM (HR STEM) was performed on MEPANPt, PANPt and PANPd, using the same sample preparation mentioned above. The STEM investigations were performed on the aberration-corrected HD-2700CS (Hitachi; cold-field emitter), operated at an acceleration potential of 200 kV. A probe corrector (CEOS) is incorporated in the microscope column between the condenser lens and the probe-forming objective lens providing excellent high-resolution capability (beam diameter ca. 0.1 nm in the selected ultra-high resolution mode). Images (1024 × 1024 pixels) were recorded with a HAADF detector with frame times of ca 15 s. These imaging conditions give rise to atomic number (Z) contrast, a highly sensitive method to detect atoms of strongly scattering elements (high Z) on light supports. The HR STEM micrographs can be find in the SI.

The extent of Pd and Pt incorporation in all latexes were measured by ICP-OES and performed on the solid polymer obtained from drying each latex in vacuum. The stoichiometry of the metal complex resulting from the chemical entrapment mechanism was investigated by ICP-OES on F1b synthesis to analyze Cl in the remaining water phase after the polymerization. The latter was obtained by adding 3 g

of a 0.1 M MgSO4 aqueous solution to 4 g of the synthesized latex and centrifuging until the polymer was fully deposited on the bottom. The water phase was then extracted, filtered with a 0.1 μm syringe filter and diluted to reach a maximum of 35 ppm chlorine. This procedure was repeated using two different batches of the same synthesis type for each case (F1b, Pd and Pt-incorporation).

NMR titration studies were performed to investigate possible complex formation of AN with various metal salts at 298 K. A stock solution of AN (6.3 mM) either with K_2PdCl_4 (2.4 mM) or with K_2PtCl_4 (2.4 mM) in DMSO-d_6 was prepared gravimetrically. The titration experiments were performed by stepwise addition of K_2PdCl_4, K_2PtCl_4 or AN to the respective stock solution. ^{1}H and ^{13}C NMR spectra were recorded on a Bruker DRX 400 spectrometer. Chemical shifts are reported relative to the residual solvent signal (DMSO-d_6, δ_H = 2.50 ppm, δ_C = 39.50 ppm).[50] As a reference, tetramethylsilane (TMS, δ = 0 ppm) was used as internal standard to monitor the effect of the complexation-induced shift of the DMSO-d_6 signals.

X-ray absorption spectroscopy (XAS) spectra at the Pd K- and Pt L_{III} absorption edge were collected at the SuperXAS beamline of the Swiss light source (PSI, Switzerland). The SLS operated at 2.4 GeV in top up mode, with a ring current of 400 mA. The polychromatic X-ray beam resulting from the 2.9 Tesla bending magnet was collimated by a collimating mirror, monochromatized by a Si(111) channel cut monochromator for measurements at the Pt L_{III} edge and a Si(311) channel cut monochromator for measurements at the Pd K-edge and subsequently focused by a toroidal mirror. The spot size on the sample measured 2 x 0.4 mm (H x V). On both mirrors a Rh coating was selected for measurements at the Pt L_{III} edge and a Pt coating for measurements at the Pd K-edge. The energy was calibrated by measuring a Pt foil at the Pt L_{III} edge and setting the monochromator energy to 11564 eV at the inflection point of the absorption edge, or by setting the monochromator energy to 24350 eV at the inflection point of a Pd foil. Samples were measured in transmission mode using 20 cm long ionization chambers (filled with N_2 for measurements at the Pt L_{III} edge or a mixture of Ar and N_2 for measurements at the Pd K-edge). PANPd, PANPt and MEPANPt were pressed in the form of pellets for analysis, while Pd and Pt foils were simultaneously measured as absolute reference. As polymers might get damaged by X-ray radiation, we introduced a liquid nitrogen cryojet that cooled the sample continuously to 150 K. The Pd

samples were measured in fluorescence mode using a silicon drift detector (Vortex) with a 1 mm thick sensor. The Pt samples were measured in transmission mode within a minute. Fitting was performed using the Demeter software package. [51] All spectra were background corrected and normalized. The energy units (eV) were then converted to photoelectron wave vector k units ($Å^{-1}$) by assigning the photoelectron energy origin, E_0, corresponding to $k = 0$, to the first inflection point of the absorption edge. The resulting $\chi(k)$ functions were weighted with k^3 and then Fourier-transformed to obtain pseudo radial structure functions (RSFs). The amplitude reduction factor was obtained from fitting a Pd or Pt-foil, i.e., 0.814 ± 0.038 and 0.800 ± 0.031, respectively. The final fit was made over the 1-3.7 (PANPd) and 1.05-3.5 (PANPt) Å range by using the structures of metallic Pt and Pd, PtCl and $PdCl_2$ for the chlorine path and for the nitrogen path PtO and PdO were used where O atoms in the structure where replaced by N atoms.

2 Results & Discussion

2.1 Physical entrapment via mini-emulsion polymerization

The aforementioned four synthesis techniques permit to target specific metal distributions in polymeric CPs. In particular, mini-emulsion enables the incorporation of platinum in PAN CPs in a highly dispersed manner. In the case of PAN, the CPs are less spherical due to the insolubility of the polymer inside the monomer. The formed polymer present in the monomer droplets precipitates and crystallizes creating “crumpled latex particles” with a degree of crystallinity of 26 %. [52] Additionally, achieving monodispersity of the CPs is less trivial than with conventional emulsion polymerization as hydrophilic acrylonitrile droplets are formed by a breakage/coagulation mechanism induced by sonication in water. [53] In fact, it was reported that adding styrene (stronger hydrophobic behavior) as co-monomer is improving the monodispersity of the obtained polymer CPs. [48] Hence, the presence of styrene is reducing the crystallinity and changing the morphology (more spherical CPs). The droplets are then polymerized when increasing the surrounding temperature, thus “freezing” the structure and embedding the metal precursor in the polymer. The size of the monomer droplets decreases upon polymerization, because of the change in density.

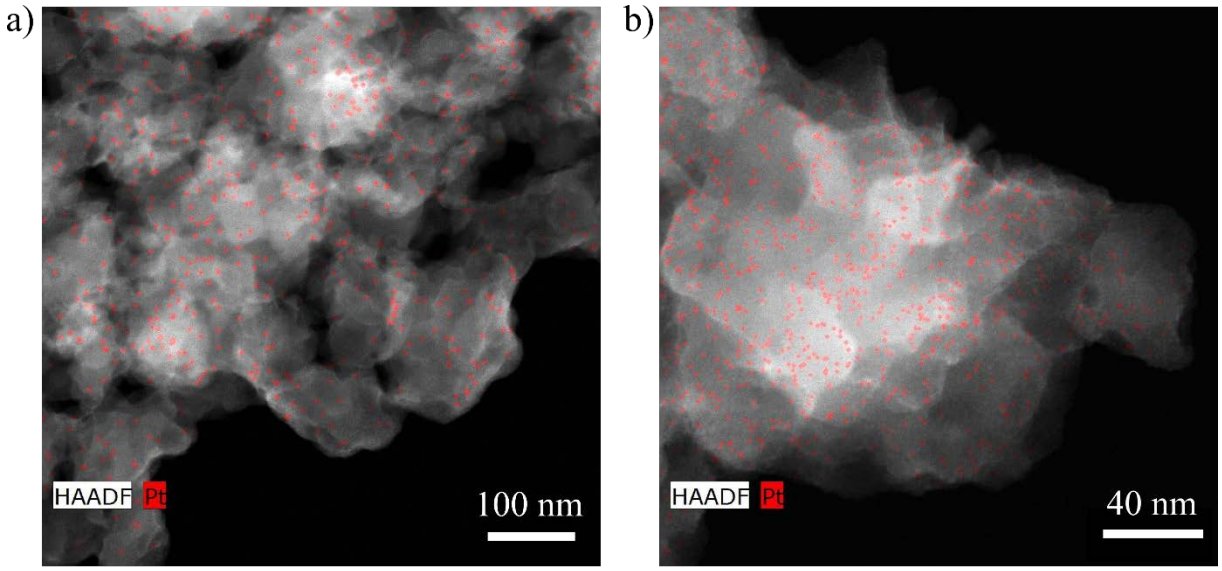

Fig. 2 STEM-EDX HAADF of MEPANPt a) overview of an aggregate (Pt Lα-lines, enhanced) b) single colloidal particle (Pt M αβ-lines, enhanced)

The difference in solubility between the solvent and the monomer is a key aspect when dealing with mini-emulsion polymerizations. [44] In this case, the procedure still works with the addition of an apolar, low boiling solvent (DCM), which leaves the reaction mixture when the polymerization starts. In order to increase the hydrophobicity even more and also to suppress Ostwald ripening among the droplets, water-insoluble hexadecane is added as co-stabilizer. [54] These particles produced by mini-emulsion are shown in Fig. 2, where the STEM-EDX (Pt M αβ lines) micrographs of a cluster of PAN CPs (Fig. 2 a)) and of an individual CP (Fig. 2 b)) are depicted. The particles are clearly non spherical, in contrast to those obtained by conventional emulsion polymerization (cf. Fig. 2 and Fig. 3).

This type of incorporation is mainly physical due to the entrapment of the metal precursor inside the oil-droplets prior to polymerization. In addition, the close-up MEPANPt micrograph in Fig. 2 b) shows clearly no big metal-aggregates (5-10 nm) in the nanoparticle, since they should be visible in STEM at this magnification as bright spots due to the difference in density between the metal and polymer. [55] To ensure the absence of even smaller aggregates (< 1 nm), High Resolution STEM (HR STEM) was performed on this material. This technique is highly sensitive and, in principle, could easily detect atoms of metal (due to strong scattering) on polymer (light support). However, in the present case, the thickness

of the polymer (many layers of carbon atoms) prevents the visibility of single Pt atoms. The micrographs with scales down to 10 and 2 nm are given in the supporting information in Fig. 6S a) and b), respectively.

2.2 Chemical entrapment via emulsion polymerization

F1 emulsion polymerizations

As compared to mini-emulsion, incorporation via emulsion polymerization permits more versatility in terms of metal dispersion in the CPs. For this purpose, three different types of synthesis were designed, as sketched in Fig. 1, with different targeted distributions, and the representative results of these syntheses are shown in the following Figs. 5, 6, 8 and 9.

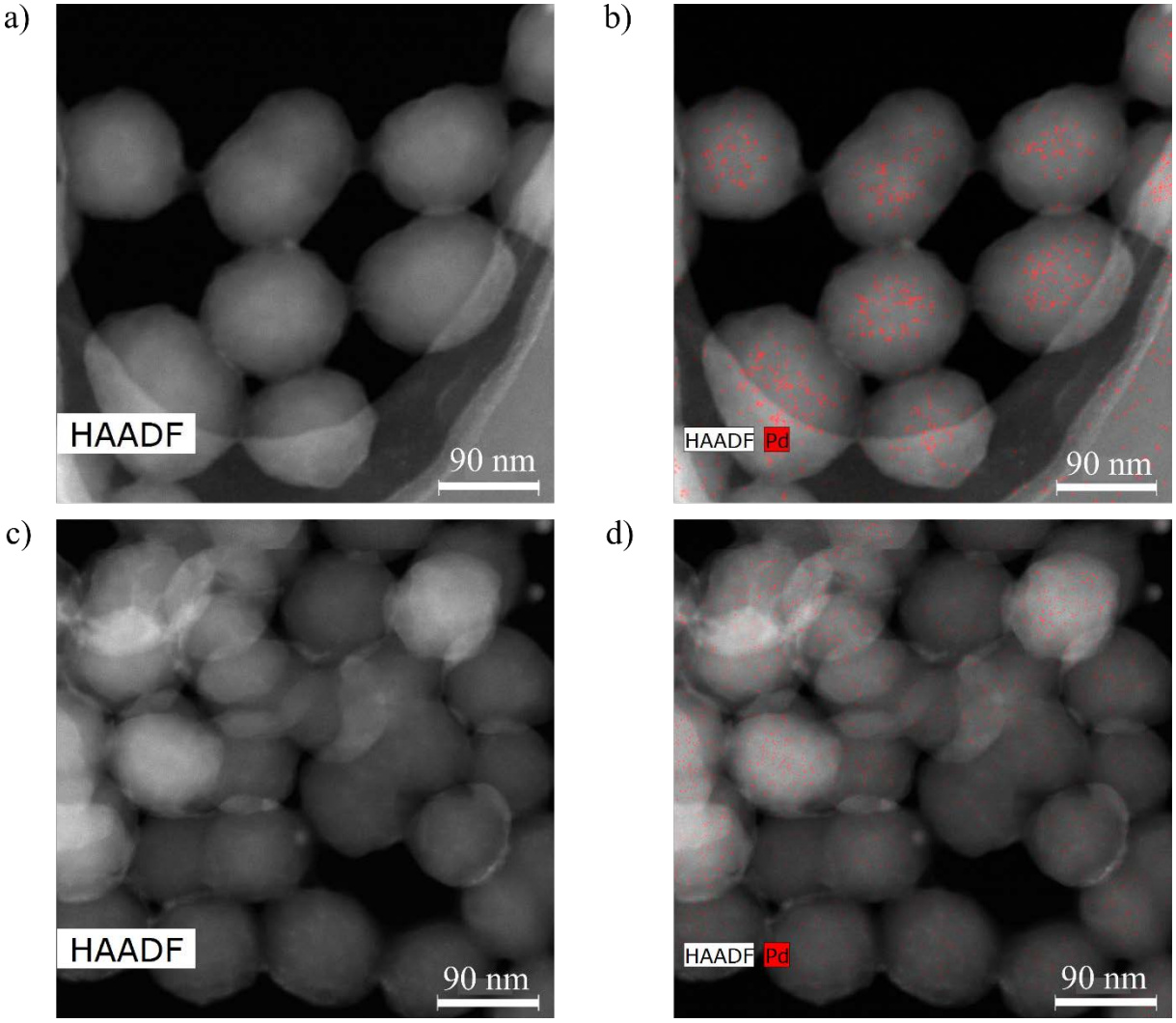

Fig. 3 a) STEM HAADF of PANPd from F1a synthesis; b) STEM-EDX HAADF of PANPd from F1a (Pd L α-lines, enhanced); c) STEM HAADF of PANPd from F1b synthesis; d) STEM-EDX HAADF of PANPd from F1b (Pd L α-lines, enhanced)

Figs. 3 and 4 represent STEM micrographs and the corresponding STEM-EDX maps from F1 syntheses for palladium and platinum, respectively. According to Figs. 3 b) and 4 b), larger metal concentration towards the center of the CPs is obtained when applying feed strategy F1a for both noble metals. As already mentioned, this technique involves the addition of the water-soluble metal-precursors when the reaction just started, *i.e.* at the nucleation onset, coupled with a very short feeding time (2 minutes). All the precursor is then quickly fed when the PAN particles are still very small, thus explaining the high concentration of the metal towards the center of the particle. The continuation of the reaction results in the growth of the polymer particles, with the formation of external polymer shells much less rich in

metal. Nonetheless, also in this case, no Pd or Pt aggregates are visible in HAADF STEM (Figs. 3 a) and 4 a)).

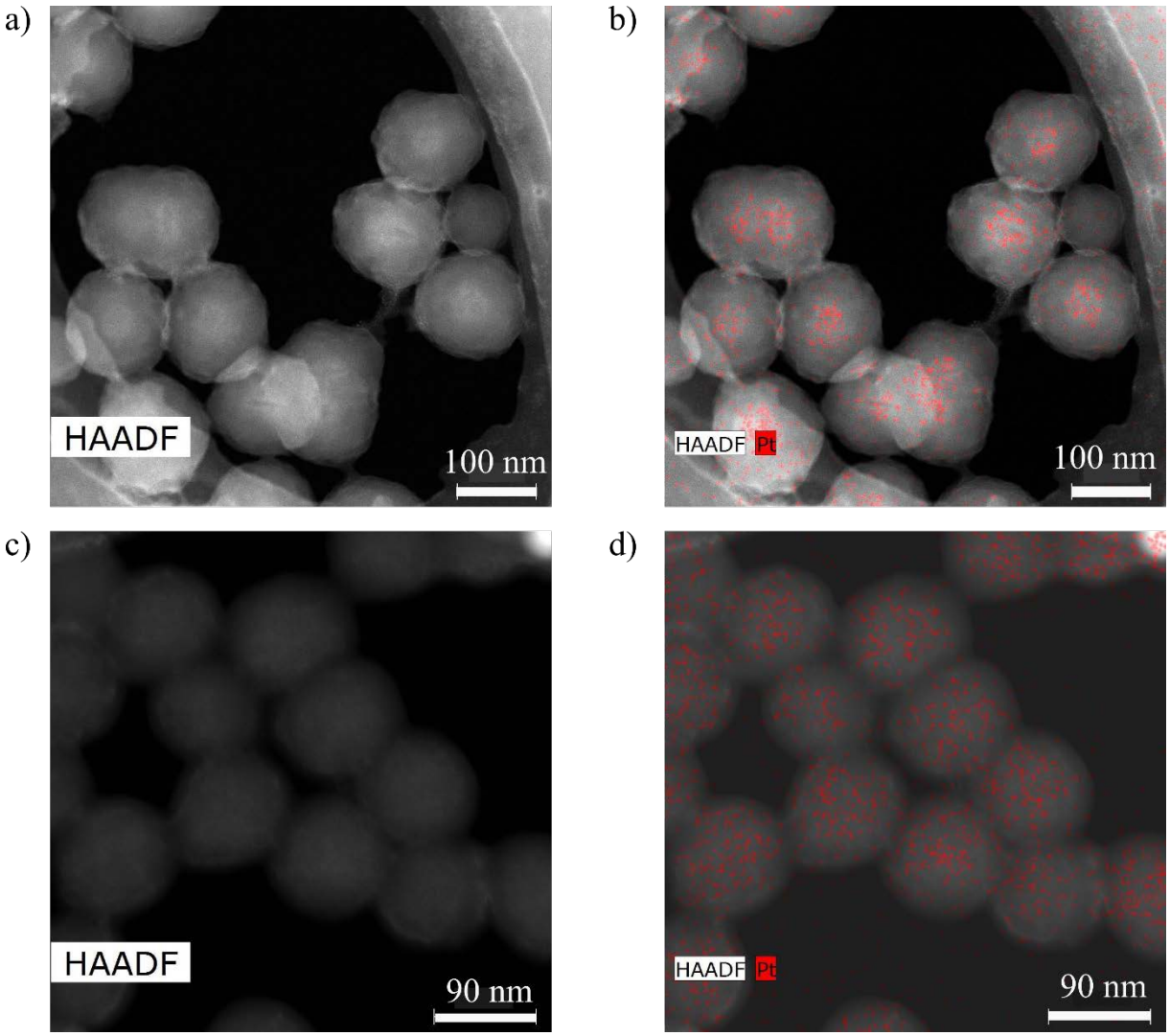

Fig. 4 a) STEM HAADF of PANPt from F1a synthesis; b) STEM-EDX HAADF of PANPt from F1a synthesis (Pt M αβ -lines, enhanced); c) STEM HAADF of PANPt from F1b synthesis; d) STEM-EDX HAADF of PANPt from F1b synthesis (Pt M αβ-lines, enhanced).

In contrast to F1a, the feeding time is prolonged to 30 minutes in F1b reactions, which allows the particles to grow during the continuous addition of metal precursor. The Pd and Pt are, in both cases, more homogeneously distributed inside the CP, as confirmed by the EDX results in Figs. 3 d) and 4 d). Batch emulsions polymerizations show usually fast reaction rates at the beginning of the reaction and decreasing rate later on. [56] Since 2 minutes of metal precursor feeding when the polymerization rate is

fast permits the successful transfer of the metal ions from the aqueous phase to the particles formed in this short time, as indicated by the feed strategy F1a, longer feeding times should result in a better distribution of the noble metal. In fact, given that 80 % of monomer conversion was usually achieved after 1 h polymerization, a feeding time of 30 minutes was sufficient to allow a successful and homogeneous metal incorporation. Unfortunately, in the case of Pd, feeding in the slow rate region (after 1 hour reaction) leads to the formation of black solid aggregates, similarly to the case of mini-emulsion with $Pd(acac)_2$.

Like in the case of MEPANPt, HR STEM was also performed for PANPd and PANPt CPs. Here again, the high resolution does not permit to visualize any aggregates in the case of PANPd and probably some Pt atoms in the case of PANPt. The results (micrographs etc.) can be find in the SI as Fig. 7S.

F2 emulsion polymerizations

In the previous section, we have shown that feeding the metal-precursors during the polymerization to a reactor initially containing the monomer is an effective approach to the incorporation of palladium and platinum in the PAN CPs. On the other hand, using the opposite feed strategy F2 with metal-precursor charged first and the monomer fed right after, cf. Fig. 1, another type of metal distribution inside the CPs was achieved. The first trial was performed at 4 % SC based on the recipe in Table 2 (recipe A) and the results are shown in Fig. 5.

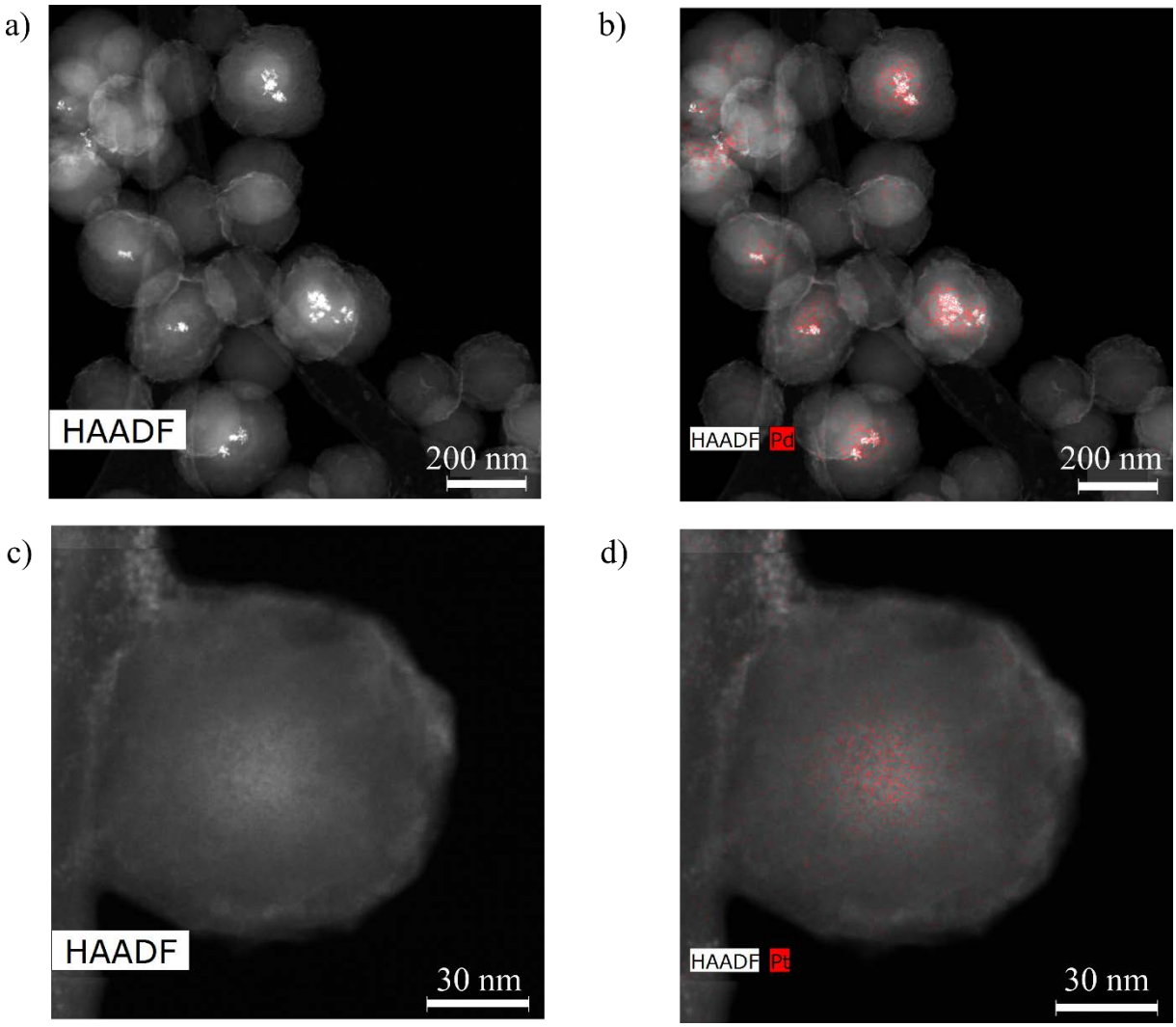

Fig. 5 For the synthesis F2 A at 4 % SC a) STEM HAADF of PANPd; b) STEM-EDX HAADF of PANPd, (Pd L α-lines); c) STEM HAADF of PANPt; d) STEM-EDX HAADF of PANPt, (Pt M αβ-lines, enhanced).

The STEM micrograph of the PANPd CPs from F2 A synthesis in Fig. 5 a) shows clearly the presence of a relative large (20-30 nm based on the STEM micrograph) metallic core in the center of the particles. Applying EDX hypermapping on this sample, such aggregates were identified to be made of Pd (Fig. 5 b)). It has to be mentioned that these Pd aggregates were present in approximately 40 % of the observed polymer CPs, while for the remaining 60 %, the Pd amount seems lower but better distributed in space. The large Pd clusters in the center of the particles were evidently formed before feeding the monomer and most probably imputable to the low stability of the Pd-precursor in water, which will be further discussed later on. On the other hand, when using the metal-precursor K_2PtCl_4, no sign of formation of

metal aggregates was visible before feeding the monomer and, in fact, no metal clusters are visible in the center of the particles, as shown in Fig. 5 c). One can recognize that the brightness in the particle center is higher and decreases towards the particle surface: since such brightness corresponds to the metal, as proved by the EDX result in Fig. 5 d), the results from F2 B synthesis in this case are similar to those previously achieved in case F1a.

For the sake of comparison, F2 synthesis was also performed at 10 % SC, the same solid content of F1 syntheses. The corresponding STEM and EDX results are shown in Fig. 6 a) and b) for palladium and c) and d) for platinum. Interestingly, the Pd clusters are practically present in all the polymer CPs in this case but they are smaller in size, as shown in Fig. 6 a), as indicated by the brighter "point" in the center of each CP. The same metal aggregates exhibited a diameter of about 20 nm in the case of the F2 synthesis at 4 % SC, as shown in Fig. 5 a).

For the precursor K_2PtCl_4 and using the F2 feeding strategy at both 4 % and 10 % SC, no visible Pt nanoparticles could be found in the center of the particles, as shown in Fig. 5 c) and 7 c), further confirming the good stability of K_2PtCl_4 in water. However, the Pt distributions observed by STEM-EDX in Fig. 5 d) and 7 d) at the two SCs are different. At 4 % SC, the Pt distribution is similar to that obtained in case F1a as shown in Fig. 5 b). On the other hand, at 10 % SC, the CP size distribution is quite broad and the Pt content is much larger and more centered in the larger particles, thus resembling the case F1a. The metal distribution is instead more uniform inside the smaller particles, thus resembling the case F1b.

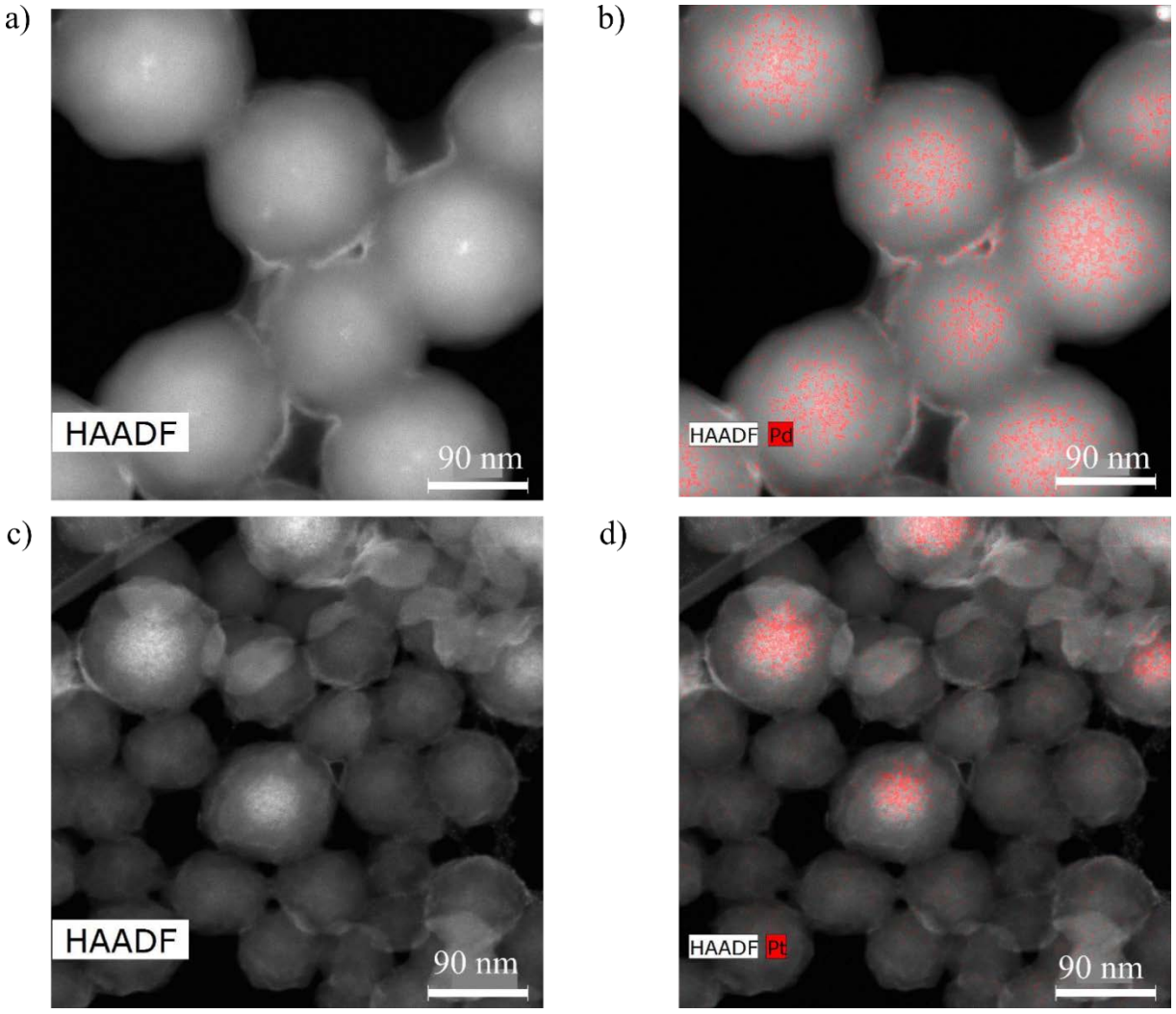

Fig. 6 For the synthesis F2 B at 10 % SC a) STEM HAADF of PANPd; b) STEM-EDX HAADF of PANPd, (Pd L α-lines); c) STEM HAADF of PANPt; d) STEM-EDX HAADF of PANPt, (Pt M αβ-lines, enhanced)

Since the size of the Pd nanoparticles inside the PAN CPs decreases as the SC increases, at least two competitive processes are active in the system: aggregation among the molecules of Pd precursor, K_2PdCl_4, due to their low stability in water, and complexation of K_2PdCl_4 with the monomer. Accordingly, at higher SC, since the monomer feeding is faster, the complexation between precursor and monomer is faster, and the aggregation among K_2PdCl_4 molecules is hindered. In the case of platinum, since the metal-precursor K_2PtCl_4 is stable in water, no aggregation competes with the complexation between precursor and monomer and, therefore, the monomer feeding affects only the

complexation process. In the case of 10 % SC, the monomer can complex the larger amount of K_2PtCl_4, thus forming PAN CPs with larger metal contents. If the polymer latex is stable enough, further AN addition would lead to the growth of external polymer shells at much lower Pt content, thus explaining the results in Fig. 6d).

To verify the different stability in the water phase mentioned above for the two metal-precursors, K_2PtCl_4 and K_2PdCl_4, their aggregation behavior in water was studied as a function of temperature using DLS. The corresponding values of the hydrodynamic diameter (d_p) and the count rate of the scattered light (Counts) are depicted in Fig. 7 a) and b) for K_2PtCl_4 and K_2PdCl_4, respectively. All the data are the average of three measurements at each temperature. As shown in Fig. 7 a) in the case of K_2PdCl_4, starting around 30 °C, both d_p and Counts increase as the temperature increases, and the increase in d_p is especially fast after 40 °C. Notably, both variables decrease after reaching a maximum value, around 50 °C and this reflects the sedimentation of big K_2PdCl_4 aggregates on the bottom of the cuvette, no longer detectable by the laser.

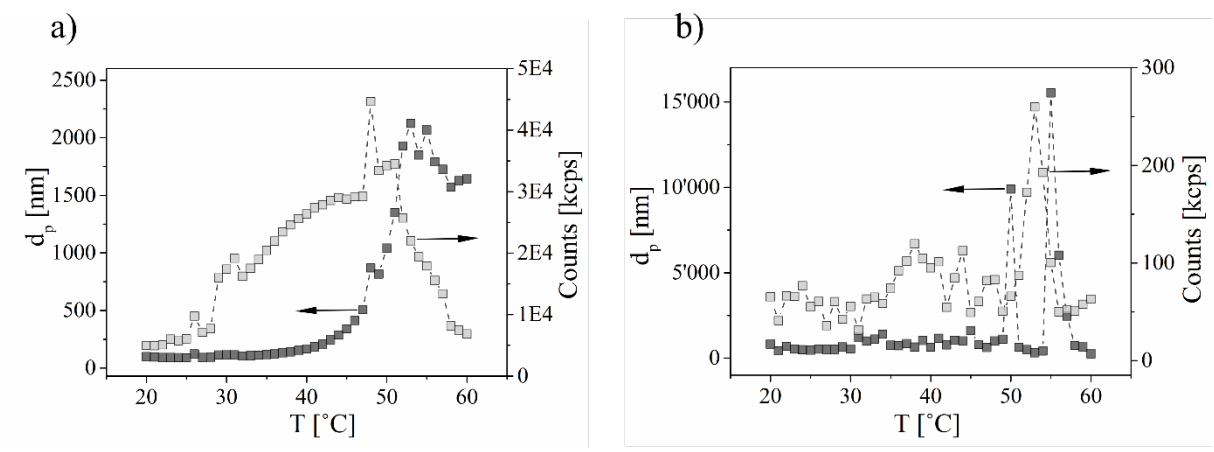

Fig. 7 Aggregation behavior: hydrodynamic diameter, d_p (dark gray squares), and count rate of the scattered light, Counts (light grey squares), measured by DLS, as a function of temperature for a) K_2PdCl_4 and b) K_2PtCl_4 dissolved in water.

On the other hand, in the case of the K_2PtCl_4 solution, Fig. 7 b), the average size stays constant over the entire range of experimented temperatures, from 20 to 60 °C. Moreover, the count rate stays low, about two orders of magnitude lower than in Fig. 7 a). There are few points that lie higher than the rest, but they are rather random, resulting from presence of some dusts and other contaminations. These results

clearly indicate that no aggregation takes place in the case of K_2PtCl_4, which is not the case for K_2PdCl_4, and confirm the largely different stability of the two metal-precursors in water, as discussed above.

The fact that the water-soluble precursor is able to be embedded and distributed inside the polymer CPs is a clear indication that chemical bonding between precursor and monomer occurs, thus leading to chemical entrapment of the metal. In particular, when AN is charged initially and the water soluble precursor is fed (F1 feed strategy), the entrapment seems to indicate that the distribution of noble metal inside the CPs is in the form of single atoms, due to the absence of visible metallic aggregates by STEM and HR STEM. To elucidate the chemical entrapment mechanism and support the assumption of single atoms of metal inside the CPs, a mass balance of the Cl content of the initial noble metal precursors (K_2PdCl_4 and K_2PtCl_4) was performed by analyzing the aqueous phase of the latexes. The obtained stoichiometry showed that 2.95 ± 0.01 Cl equivalent out of 4 stay in aqueous phase in the case of K_2PdCl_4, while only 2.36 ± 0.04 Cl equivalent out of 4 were observed in the case of K_2PtCl_4. First of all, this result confirms that Cl atoms of the initial precursors have been exchanged during the polymerization. Given the good electron donor properties of the N atoms, the monomer itself is the most probable ligand replacing Cl, binding to Pd or Pt via the cyanide group. Secondly, the measured Cl equivalent remaining in water could be the result of the average exchange out of the five possible configurations sketched for Pd in Fig. 8 a) (and valid also for Pt). Note that the possible chemical structure of the complex with Pd (or Pt) is proposed in Fig. 8 b). The circles indicate possible active sites for polymerization, which starts in the water phase and, due to the increased hydrophobicity while the chain length is growing, enters micelles or formed particles and continue the polymerization in their organic core. This metal-containing monomer should definitely hinder any further formation of Pd-Pd or Pt-Pt bonds.

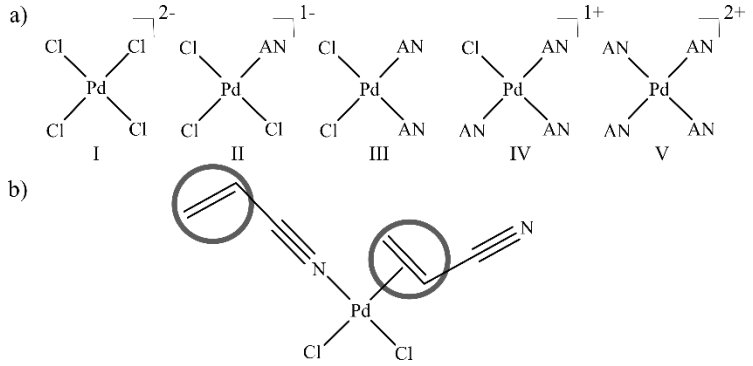

Fig. 8 a) Possible configurations of the complexes (I-V) of Pd with AN; b) example of complex chemical structure, where the circles indicate possible starting sites for radical polymerization.

In order to identify the structure and stoichiometry of the formed complex between AN and the metal precursors, NMR-titrations in DMSO-d^6 were performed by charging initially AN and feeding the metal-precursor. A shift was observed but no saturation binding of AN on the metal precursors was identified. This suggests a fast and continuous ligand exchange, consequently the shift, as the metal-precursor is fed in the NMR tube (more information in SI). Therefore, the monomer is indeed binding to the metal precursors and all the complex configurations seem to be present in the system. However, given the complexity of the system – different bonding sites, possible interactions with the solvent, fast dynamic equilibrium that prevents saturation, different possible configurations (Fig. 8 a)) – further characterization work is required to better identify such complexes.

2.3 Characterization of single metal-sites

The lack of aggregates observed in HR STEM micrographs for mini-emulsion and F1b synthesis as well as the proof of noble metal complexation (by NMR for AN, by ICP-OES for the remaining Cl in solution) are two good indicators of the presence of single metal atoms in our material. In order to better substantiate this expectation, X-ray absorption studies were performed. Fitting of EXAFS spectra permits to identify the nearest neighbors of Pd and Pt atoms, their bond distance and their average coordination number, while XANES spectra yield information on the empty density of states (oxidation state). Fig. 9 a) and b) show a zoom of the Pd K-edge and the Pt L_{III}-edge XANES spectra, respectively.

In Fig. 9 a) the whiteline of PANPd is more intense than that of Pd-foil (reference sample is bulk Pd(0)), which suggests that Pd in the PANPd has a higher oxidation state, probably Pd(II) as in the precursor.

Additionally the shape of the PANPd spectra corresponds to reported Pd(II) K-edge samples . [57] In the case of the platinum-based samples in Fig. 9 b), the three samples have different intensities, but no shift is observed in the position of the edge. Those different intensities in the whitelines likely results from different electron density of the metal atoms, for example due to strong interactions between the ligands (charge transfer). [58] Unexpected at first glance is the highest intensity of MEPANPt with respect to PANPt, as both precursors, even if chemically different, had the same oxidation state Pt(II). There are several possible explanations for this observation, like differences in transition states or near neighbor distances or particle size effects. [59,60] However, based on the physical entrapment mechanism of MEPANPt, the most probable explanation for the higher whiteline intensity is the weak or inexistent interaction with the polymer as compared to PANPt. Moreover, the bond Pt-O (from $Pt(acac)_2$) and Pt-Cl (from K_2PtCl_4) are both stable, hence no differences should emerge from the initial ligands. [61] Thus, the Pt(II) atoms from MEPANPt have a lower electron density than Pt(II) in PANPt as the latter interact with the polymer.

The corresponding Fourier transformed EXAFS spectra are reported in Fig. 9 c) and d) for palladium and platinum, respectively. The PANPd and PANPt spectra were fitted using models involving N and Cl as first shell neighbor and a second metal or carbon shell neighbor depending on the sample. The best fits are indicated by purple dotted lines and the best fit parameters are listed in Table 3.

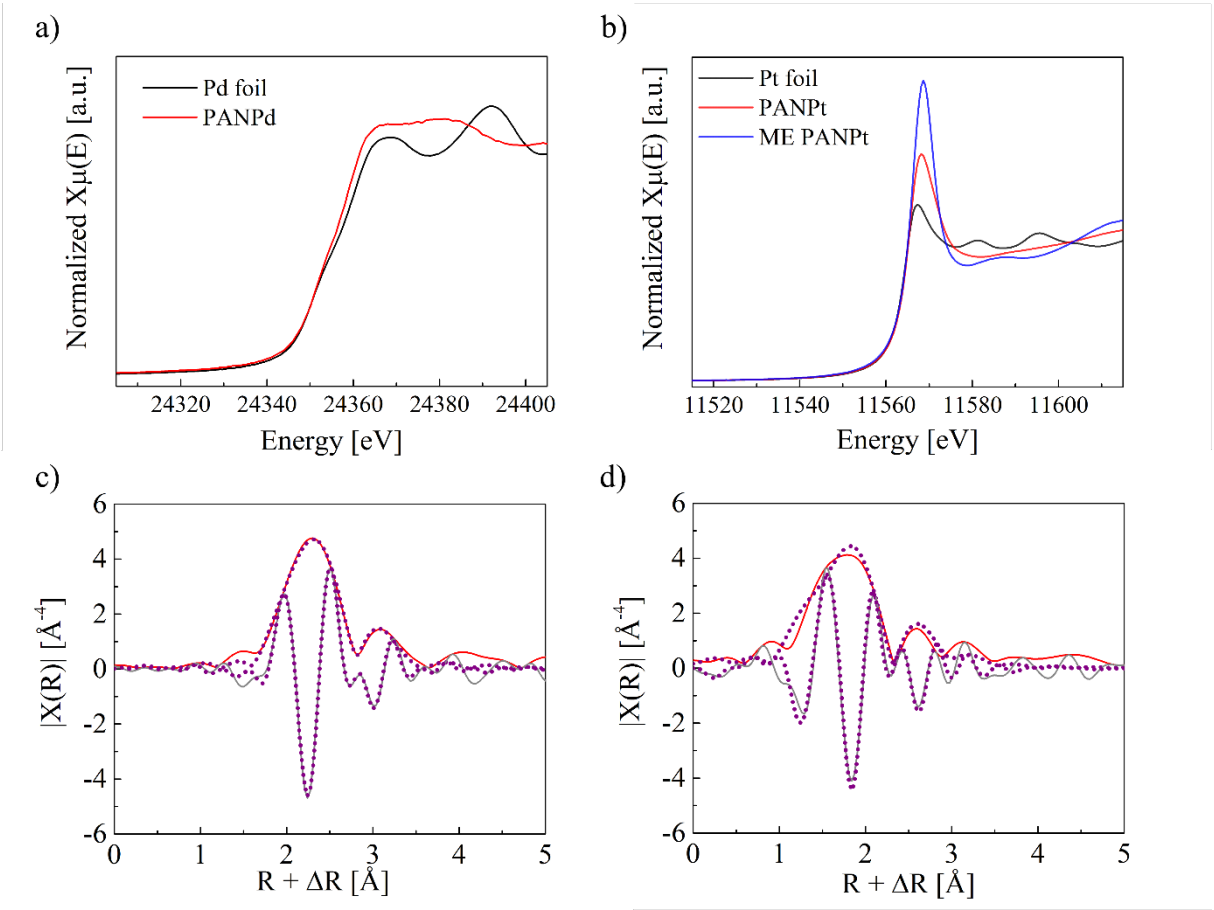

Fig. 9 X-ray absorption studies a) normalized Pd K-edge XANES spectra of PANPd (red) and Pd foil (black) b) normalized Pt L_{III}-edge XANES spectra of PANPt (red), MEPANPt (blue) and Pt foil (black); Fourier transformed k^3-weighted EXAFS spectra with the imaginary part (grey) and magnitude (red) (both uncorrected for phase shift) of c) PANPd with corresponding fitting (purple dotted line) d) PANPt with corresponding fitting (purple dotted line).

The bond Pd-Cl was chosen based on the precursor used for F1a and b syntheses (K_2PdCl_4 and K_2PtCl_4). The Fourier transformed and fitted k^2-weighted EXAFS spectra of the metal foils can be found in Fig. 12S in the SI.

Table 3. Best fit parameter values for the EXAFS spectra of PANPd (N, Cl, Pd) and PANPt (N, Cl, C).

Sample	Shell	Bond length [Å]	Number of nearest neighbors [-]	Debye Waller factor [Å^2]	ΔE0	R-factor
PANPd	Pd-O/N	2.03 ± 0.06	1.2 ± 1.0	0.001*	8.9 ± 3.5	0.010
	Pd-Cl	2.31 ± 0.05	3.0 ± 1.0	0.010*	4.8 ± 6.0	
	Pd-Pd	2.74 ± 0.05	1.6 ± 1.4	0.011*	8.9 ± 3.5	
PANPt	Pt-O/N	1.86 ± 0.04	0.9 ± 0.4	0.002*	-0.2 ± 11.0	0.002
	Pt-Cl	2.25 ± 0.04	3.3 ± 0.5	0.010*	5.7 ± 7.0	
	Pt-C	3.23 ± 0.08	3.7 ± 1.8	0.001*	-0.2 ± 11.0	

*Fixed Debye Waller factor (values were determined from fitting shells individually with floating Debye Waller factor's), ΔE0 is the shift of the potential between the model and the data where only one value was taken because two scattering paths came from the same structure

As shown in Fig. 9 c), the FT EXAFS spectra have a main peak between 1-2.2 Å (uncorrected for phase shift) that was best fitted with N and Cl neighbors. A second peak is visible next to the main one, and based on the best fitting results of PANPd in Table 3; this peak corresponds to an average of Pd-Pd dimers and trimers (1.6 ± 1.4 number of nearest neighbors). Moreover, the data suggest that on average one Pd atom is coordinated to three Cl atoms and one N atom, which corresponds to configuration II in Fig. 8 a). The FT EXAFS spectra of the PANPt are depicted in Fig. 9 d). From best fitting of the first shell of PANPt, we obtain Pt-N and Pt-Cl bonds with coordination numbers of 0.9 ± 0.4 and 3.3 ± 0.5, respectively. A small second peak is observed around 2.8 Å. The data range available is too limited to get a perfect fit of this peak but, as we know the raw materials used in the synthesis, two different possibilities are expected: C (bridged to the N of the cyanide group) or Pt. Only a Pt-C scattering path could be fitted. Accordingly, and in agreement with the results of the other characterizations, the EXAFS data suggest that Pt exists predominantly as isolated atoms. The EXAFS spectra of MEPANPt (Fig. 14S in SI) show the absence of a Pt-Cl path since we used a Cl-free precursor, $Pt(acac)_2$. As EXAFS can not distinguish N from O, we do not know if the oil-soluble precursor is also binding to the nitrogen of polyacrylonitrile, but, based on the physical entrapment procedure and the XANES spectra, we expect to have mostly Pt-O paths.

These results are in line with the instability of K_2PdCl_4 in water in comparison with K_2PtCl_4 while

increasing the temperature up to the 60 °C (Fig. 7 a) and b)). In fact, during feeding of the precursor, the aggregation of $[PdCl_4]^{2-}$ to dimers or triplets cannot be completely avoided, despite the fast complexation. On the other hand, $[PtCl_4]^{2-}$ stays completely stable towards aggregation and hence results in a dominant single atom incorporation.

2.4 **Incorporation efficiency and monomer conversion**

A quantitative analysis of the polymer was also performed by ICP-OES on each synthesized latex. All latexes were synthesized twice and the results are summarized in Table 4. Moreover, prior to analysis, the latexes were at least one week old such that the reported results account for possible leaching of the metal over time.

Table 4. Extent of incorporation and conversion of Pt or Pd in polyacrylonitrile measured by ICP-OES for all types of synthesis (2 repetitions)

Metal	Synthesis types	Incorporation [wt.%]	Latex Conversion [%]
Platinum	MEPAN	97.9 ± 1.2	92.6 ± 2.0
	F1a	96.5 ± 3.5	89.5 ± 5.2
	F1b	87.9 ± 3.2	94.2 ± 4.3
	F2 B (10%)	83.9 ± 9.5	98.4 ± 0.8
	F2 A (4%)	98.96 ± 5.9	94.7 ± 5.2
Palladium	F1a	88.4 ± 2.4	95.2 ± 2.4
	F1b	90.8 ± 3.0	98.5 ± 1.5
	F2 B (10%)	89.9 ± 5.6	93.0 ± 3.3
	F2 A (4%)	88.7 ± 6.0	82.4 ± 0.1

A first, general observation from Table 4, is the good incorporation of metals for all types of synthesis. In addition, the conversion is also always reaching almost 90% or more. The incorporation errors for F2 synthesis for Pd and Pt are slightly higher than the rest and are due to less homogeneous distribution of the noble metals inside each polymer CPs.

2.5 Metal incorporation into pre-formed PAN colloidal particles

As a direct comparison to the incorporation approach developed in this work, K_2PdCl_4 was added to a preformed PAN latex. Thanks to the basicity of N in the polymer matrix, partial diffusion of Pd inside the PAN CPs was taking place along with an almost instantaneous black coloration, which could be the result of residual monomer reacting with the Pd-salt. The final picture is shown in Fig. 10, where an overview of the polymer particles assessed by STEM HAADF (Fig. 10 a)) and a closer STEM HAADF Pd-EDX mapping of several individual polymer CPs (Fig. 10 b)) are reported. In the overview micrograph, quite large Pd nanoparticles (approximately 50 nm) are visible as brighter spots distributed over the sample. Such Pd nanoparticles, clearly located outside the polymer, were never observed for all three types of chemical entrapment applied in this work. Thus, post-synthesis incorporation is definitely not effective and resulted in a much larger loss of Pd than in the case of incorporation performed during the polymerization.

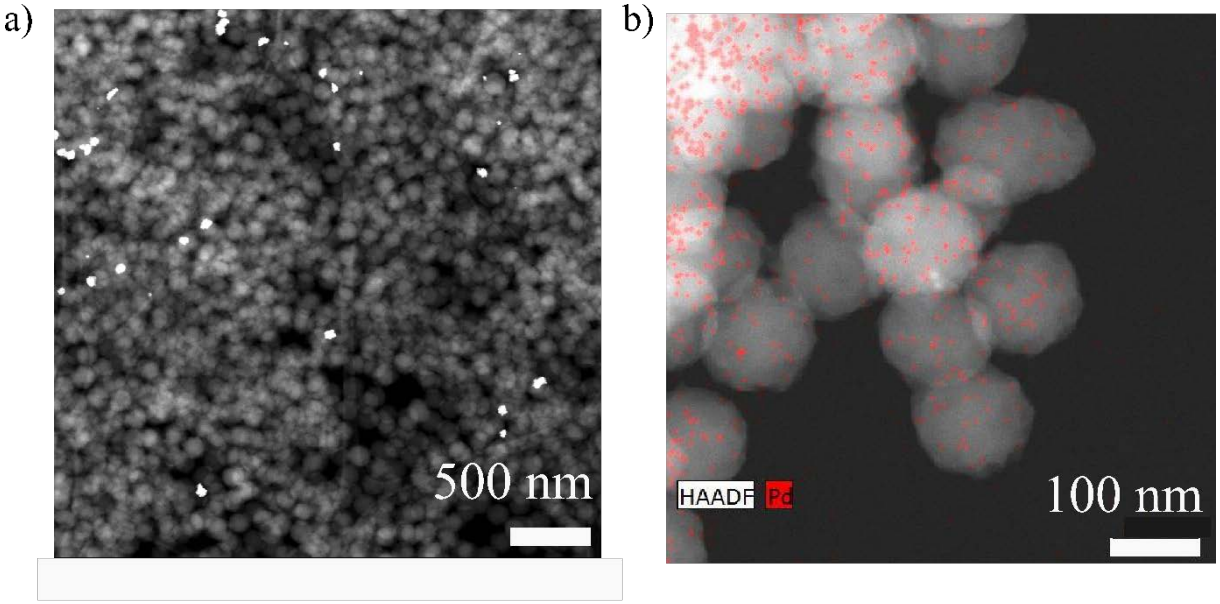

Fig. 10 a) STEM HAADF of Pd incorporated in preformed PAN CPs; b) STEM-EDX HAADF of Pd incorporated in preformed PAN CPs (Pd L α-lines, enhanced)

3 Conclusions

In this work, different synthesis routes are described to incorporate noble metals inside PAN colloidal particles and result in different spatial distribution. Mini-emulsion polymerization permits the physical incorporation of Pt(II) with very homogeneous spatial distribution and small size scale, as evidenced by the absence of brighter spots in HR STEM. Conventional emulsion polymerization enables a similar incorporation of Pt(II) and Pd(II) in the PAN CPs but via a chemical entrapment mechanism. This technique results in spherical CPs and allows more versatility with respect to the spatial distribution of the metal. In fact, the distribution of the incorporated atoms can be tuned by varying the feed strategy of different ingredients. While F1a strategy resulted in a more centered distribution of metal-ions without sign of aggregate formation, F1b strategy results in a more homogeneous distribution. In both Pt and Pd incorporations, there are strong indications of the presence of single site atoms or extremely small aggregates, as evidenced again by the absence of brighter spots in the HR STEM but also by the formation of the metal complexes when the monomer and metal precursor are mixed, proven by NMR titration and residual Cl atoms inside the reaction water. Based on the EXAFS analysis, the presence of Pd in the polymer is (in average) in the form of dimers or trimers while Pt exists predominantly as isolated atoms. Finally, in F2 strategy, Pt and Pd incorporations result in different outcomes. Pd-based synthesis exhibits a STEM-visible 20-30 nm metallic nanoparticle in the center of the PAN CPs: this is the result of aggregation of the metal precursor at the reaction temperature followed by polymer growth around these “nuclei”. On the other hand, Pt synthesis did not show any sign of formation of metal nanoparticles its spatial distribution results in a mixture of F1a and b. To conclude, the methodologies proposed in this work are effective to incorporate metals in polymer particles with very high segregation among the inorganic entities and provide different spatial distributions.

4 Acknowledgments

The authors acknowledge the financial support from the Swiss National Science Foundation (Grant No. 200020_165917). The authors thank the Swiss Light Source for the provision of beamtime at the SuperXAS beamline. Additionally, the authors thank Dr. Frank Krumeich for the HR STEM measurements, Dr. Simone Gelosa for the ICP-OES measurements of Pd and Pt, Leslie Riwar for discussions on NMR-titrations and Saravanan Janakiram for preliminary experiments.

5 References

(1) Dapsens, P. Y.; Kusema, B. T.; Mondelli, C.; Pérez-ramírez, J. Gallium-Modified Zeolites for the Selective Conversion of Bio-Based Dihydroxyacetone into C 1 – C 4 Alkyl Lactates. *J. Mol. Catal. A Chem.* **2014**, *388-389*, 141–147.

(2) Tamayo, L.; Azócar, M.; Kogan, M.; Riveros, A.; Páez, M. Copper-Polymer Nanocomposites: An Excellent and Cost-Effective Biocide for Use on Antibacterial Surfaces. *Mater. Sci. Eng. C* **2016**, *69*, 1391–1409.

(3) Hai, L.; Tang, J. A Metal – Organic Framework Based Nanocomposite with Co-Encapsulation of Pd @ Au Nanoparticles and Doxorubicin for pH- and NIR-Triggered Synergistic. *J. Mater. Chem. B* **2017**, *5*, 4648–4659.

(4) Cai, H.; Shen, T.; Zhang, J.; Shan, C.; Jia, J.; Li, X.; Liu, W.; Tang, Y. A Core-Shell Metal-Organic-Framework (MOF)-Based Smart Nanocomposite for Efficient NIR/H2O2-Responsive Photodynamic Therapy against Hypoxic Tumor Cells. *J. Mater. Chem. B* **2017**, *5*, 2390–2394.

(5) Jin, L.; Zeng, G.; Wu, H.; Niederberger, M.; Morbidelli, M. A Poly-(styrene-Acrylonitrile) Copolymer-Derived Hierarchical Architecture in Electrode Materials for Lithium-Ion Batteries. *J. Mater. Chem. A Mater. energy Sustain.* **2016**, *4*, 11481–11490.

(6) Kalita, H.; Pal, P.; Dhara, S.; Pathak, A. Fabrication and Characterization of Polyvinyl Alcohol / Metal (Ca , Mg , Ti) Doped Zirconium Phosphate Nanocomposite Fi Lms for Scaffold-Guided Tissue Engineering Application. *Mater. Sci. Eng. C* **2017**, *71*, 363–371.

(7) Sci, C.; Conte, M.; Lopez-sanchez, J. A.; He, Q.; Morgan, D. J.; Ryabenkova, Y.; Bartley, J. K.; Carley, A. F.; Taylor, S. H.; Kiely, C. J.; Hutchings, G. J. Modified Zeolite ZSM-5 for the Methanol to Aromatics Reaction. *Catal. Sci. Technol.* **2012**, *2*, 105–112.

(8) Matsuoka, M.; Anpo, M. Local Structures , Excited States , and Photocatalytic Reactivities of Highly Dispersed Catalysts Constructed within Zeolites. *J. Photochem. Photobiol. C Photochem. Rev.* **2003**, *3*, 225–252.

(9) Perot, G.; Guisnet, M. Advantages and Disadvantages of Zeolites as Catalysts in Organic Chemistry. *J. Mol. Catal.* **1990**, *61* (2), 173–196.

(10) Yang, S.; Lin, X.; Blake, A. J.; Thomas, K. M.; Hubberstey, P.; Champness, N. R.; Schröder, M. Enhancement of H2 Adsorption in Li+ -Exchanged Co-Ordination Framework Materials. *Chem. Commun.* **2008**, *7345* (46), 14–17.

(11) Tuel, A. Modification of Mesoporous Silicas by Incorporation of Heteroelements in the Framework. *Microporous Mesoporous Mater.* **1999**, *27*, 151–169.

(12) Yuan, Z.; Eden, M. R. Toward the Development and Deployment of Large-Scale Carbon Dioxide Capture and Conversion Processes. *Ind. Eng. Chem. Res.* **2016**, *55*, 3383–3419.

(13) Furusawa, H.; Sekine, T.; Ozeki, T. Hydration and Viscoelastic Properties of High- and Low-Density Polymer Brushes Using a Quartz-Crystal Microbalance Based on Admittance Analysis (QCM-A). *Macromolecules* **2016**, *49* (9), 3463–3470.

(14) Matyjaszewski, K.; Spanswick, J. Controlled/living Radical Polymerization. *Mater. Today* **2005**, *8* (3), 26–33.

(15) Lee, S. W.; Liang, D.; Gao, X. P. A.; Sankaran, R. M. Direct Writing of Metal Nanoparticles by Localized Plasma Electrochemical Reduction of Metal Cations in Polymer Films. *Adv. Funct. Mater.* **2011**, *21* (11), 2155–2161.

(16) Dai, J.; Bruening, M. L. Catalytic Nanoparticles Formed by Reduction of Metal Ions in Multilayered Polyelectrolyte Films. *Nano Lett.* **2002**, *2*, 497–501.

(17) Yu, Z.; Liu, J.; Tan, C. S. Y.; Scherman, O. A.; Abell, C. Supramolecular Nested Microbeads as Building Blocks for Macroscopic Self-Healing Scaffolds. *Angew. Chemie Int. Ed.* **2018**, *57*, 3079–3083.

(18) Tan, M.; Shi, Y.; Fu, Z.-F.; Yang, W. In Situ Synthesis of Diblock Copolymer Nano-Assemblies via Dispersion RAFT Polymerization Induced Self-Assembly and Ag/copolymer Composite Nanoparticles Thereof. *Polym. Chem.* **2018**, No. 1, 1082–1094.

(19) Balazs, A. C.; Emrick, T.; Russell, T. P. Nanoparticle Polymer Composites : Where Two Small Worlds Meet. *Science (80-.).* **2006**, *314* (November), 1107–1111.

(20) Watson, K. J.; Zhu, J.; Nguyen, S. T.; Mirkin, C. A. Hybrid Nanoparticles with Block Copolymer Shell Structures. *J. Am. Chem. Soc.* **1999**, *121* (2), 462–463.

(21) Skaff, H.; Ilker, M. F.; Coughlin, E. B.; Emrick, T. Preparation of Cadmium Selenide - Polyolefin Composites from Functional Phosphine Oxides and Ruthenium-Based Metathesis. *J. Am. Chem. Soc.* **2016**, *124* (7), 5729–5733.

(22) Fresnais, B. J.; Berret, J.; Sandre, O.; Perzynski, R. Electrostatic Co-Assembly of Iron Oxide Nanoparticles and Polymers : Towards the Generation of Highly Persistent Superparamagnetic Nanorods **. *Adv. Mater.* **2008**, *20*, 3877–3881.

(23) Divya, K. P.; Miroshnikov, M.; Dutta, D.; Vemula, P. K.; Ajayan, P. M.; John, G. In Situ Synthesis of Metal Nanoparticle Embedded Hybrid Soft Nanomaterials. *Acc. Chem. Res.* **2016**, *49*, 1671–1680.

(24) Spatz, J. P.; Mößmer, S.; Möller, M. Mineralization of Gold Nanoparticles in a Block Copolymer Microemulsion. *Chem. - A Eur. J.* **1996**, *2* (12), 1552–1555.

(25) Sun, X.; Li, Y. Colloidal Carbon Spheres and Their Core/Shell Structures with Noble-Metal Nanoparticles. *Angew. Chemie - Int. Ed.* **2004**, *43* (5), 597–601.

(26) Oláh, A.; Hempenius, M. A.; Vancso, G. J. Synthesis, Characterization and Gold Loading of Polystyrene-Poly(pyridyl Methacrylate) Core-Shell Latex Systems. *Eur. Polym. J.* **2004**, *40* (4),

763–773.

(27) Sierra-martin, B.; Fernandez-barbero, A. Inorganic / Polymer Hybrid Nanoparticles for Sensing Applications. *Adv. Colloid Interface Sci.* **2016**, *233*, 25–37.

(28) Jeon, H. J.; You, Y.; Yoon, M. J.; Youk, J. H. Preparation of Polyacrylonitrile Nanoparticles via Dispersion Polymerization of Acrylonitrile Using a poly(N-Vinyl Pyrrolidone)-Cobalt Complex in an Aqueous System. *Polymer (Guildf).* **2011**, *52* (18), 3905–3911.

(29) Lazzari, S.; Moscatelli, D.; Codari, F.; Salmona, M.; Morbidelli, M.; Diomede, L. Colloidal Stability of Polymeric Nanoparticles in Biological Fluids. *J. Nanoparticle Res.* **2012**, *14* (6).

(30) Liu, J.; Yang, X.; Wang, K.; He, X.; Wang, Q.; Huang, J.; Liu, Y. Aggregation Control of Quantum Dots through Ion-Mediated Hydrogen Bonding Shielding. *ACS Nano* **2012**, *6* (6), 4973–4983.

(31) Bernardo, L. F. A.; Amaro, A. P. B. M.; Pinto, D. G.; Lopes, S. M. R. Modeling and Simulation Techniques for Polymer Nanoparticle Composites – A Review. *Comput. Mater. Sci.* **2016**, *118*, 32–46.

(32) Shaukat, M. S.; Zulfiqar, S.; Sarwar, M. I. Incorporation of Palladium Nanoparticles into Aromatic Polyamide/clay Nanocomposites through Facile Dry Route. *Polym. Sci. Ser. B* **2015**, *57* (4), 380–386.

(33) Romo-uribe, A.; Arcos-casarrubias, J. A.; Hernandez-vargas, M. L.; Reyes-mayer, A.; Aguilar-franco, M.; Bagdhachi, J. Progress in Organic Coatings Acrylate Hybrid Nanocomposite Coatings Based on SiO2 Nanoparticles by in-Situ Batch Emulsion Polymerization. *Prog. Org. Coatings* **2016**, *97*, 288–300.

(34) Cuenya, B. R. Synthesis and Catalytic Properties of Metal Nanoparticles : Size , Shape , Support , Composition , and Oxidation State Effects. *Thin Solid Films* **2010**, *518*, 3127–3150.

(35) Lu, J.; Elam, J. W.; Stair, P. C. Synthesis and Stabilization of Supported Metal Catalysts by Atomic Layer Deposition. *Acc. Chem. Res.* **2013**, *46* (8), 1806–1815.

(36) Rong, Y.; He, D.; Malpass-evans, R.; Carta, M.; Mckeown, N. B.; Gromboni, M. F.; Mascaro, L. H.; Nelson, G. W.; Foord, J. S.; Holdway, P.; Dale, S. E. C.; Bending, S.; Marken, F. High-Utilisation Nanoplatinum Catalyst (Pt @ cPIM) Obtained via Vacuum Carbonisation in a Molecularly Rigid Polymer of Intrinsic Microporosity. *Electrocatalysis* **2017**, *8*, 132–143.

(37) Nie, R.; Peng, X.; Zhang, H.; Yu, X.; Lu, X.; Zhou, D.; Xia, Q. Transfer Hydrogenation of Bio-Fuel with Formic Acid over Biomass-Derived N-Doped Carbon Supported Acid-Resistant Pd Catalyst. *Catal. Sci. Technol.* **2017**, *7*, 627–634.

(38) Vilé, G.; Albani, D.; Nachtegaal, M.; Chen, Z.; Dontsova, D.; Antonietti, M.; López, N.; Pérez-Ramírez, J. A Stable Single-Site Palladium Catalyst for Hydrogenations. *Angew. Chemie - Int. Ed.* **2015**, *54* (38), 11265–11269.

(39) Ong, W.; Tan, L.; Ng, Y. H.; Yong, S.; Chai, S. Graphitic Carbon Nitride (g-C3N4)-Based Photocatalysts for Artificial Photosynthesis and Environmental Remediation : Are We a Step Closer To Achieving Sustainability ? *Chem. Rev.* **2016**, *116*, 7159–7329.

(40) Han, J.; Wang, M.; Hu, Y.; Zhou, C.; Guo, R. Progress in Polymer Science Conducting Polymer-Noble Metal Nanoparticle Hybrids : Synthesis Mechanism Application. *Prog. Polym. Sci.* **2017**, *70*, 52–91.

(41) Carta, M.; Malpass-evans, R.; Croad, M.; Rogan, Y.; Jansen, J. C.; Bernardo, P.; Bazzarelli, F.; Mckeown, N. B. An Efficient Polymer Molecular Sieve for Membrane Gas Separations. *Science (80-.).* **2013**, *339* (January), 303–308.

(42) Tamai, T.; Watanabe, M.; Matsukawa, K. In-Situ Formation of Metal Nanoparticle / Acrylic Polymer Hybrid and Its Application to Miniemulsion Polymerization. *J. Appl. Polym. Sci.* **2015**, 42675.

(43) Poupart, R.; Droumaguet, B. Le; Guerrouache, M.; Grande, D.; Carbonnier, B. Gold Nanoparticles Immobilized on Porous Monoliths Obtained from Disulfide-Based Dimethacrylate : Application to Supported Catalysis. *Polymer (Guildf).* **2017**, *126*, 455–462.

(44) Landfester, K. Synthesis of Colloidal Particles in Miniemulsions. *Annu. Rev. Mater. Res.* **2006**, *36*, 231–279.

(45) Landfester, K. Polyreactions in Miniemulsions. *Macromol. Rapid Commun.* **2001**, *22*, 896–936.

(46) van Herk, A. M.; Landfester, K. *Advanced in Polymer Science: Hybrid Latex Particles*, Springer.; van Herk, A. M., Landfester, K., Eds.; Springer-Verlag Berlin Heidelberg, 2010.

(47) Aguirre, M.; Paulis, M.; Leiza, J. R. Particle Nucleation and Growth in Seeded Semibatch Miniemulsion Polymerization of Hybrid CeO2 / Acrylic Latexes. *Polymer (Guildf).* **2014**, *55* (3), 752–761.

(48) Yang, Y.; Daniels, E. S.; Klein, A. Synthesis of Polyacrylonitrile/Polystyrene Latex Particles That Contain Platinum. *J. Appl. Polym. Sci.* **2015**, *132* (18), 41933.

(49) Beltzung, A.; Klaue, A.; Colombo, C.; Wu, H.; Storti, G.; Morbidelli, M. Polyacrylonitrile Nanoparticle-Derived Hierarchical Structure for CO2 Capture. *Energy Technol.* **2017**.

(50) Fulmer, G. R.; Miller, A. J. M.; Sherden, N. H.; Gottlieb, H. E.; Nudelman, A.; Stoltz, B. M.; Bercaw, J. E.; Goldberg, K. I. NMR Chemical Shifts of Trace Impurities: Common Laboratory Solvents, Organics, and Gases in Deuterated Solvents Relevant to the Organometallic Chemist. *Organometallics* **2010**, *29* (9), 2176–2179.

(51) Ravel, B.; Newville, M. ATHENA, ARTEMIS, HEPHAESTUS: Data Analysis for X-Ray Absorption Spectroscopy Using IFEFFIT. *J. Synchrotron Radiat.* **2005**, *12* (4), 537–541.

(52) Landfester, K.; Antonietti, M. The Polymerization of Acrylonitrile in Miniemulsions: “Crumpled Latex Particles” or Polymer Nanocrystals. *Macromol. Rapid Commun.* **2000**, *21* (12), 820–824.

(53) Jansen, T. G. T.; Meuldijk, J.; Lovell, P. A.; van Herk, A. M. On the Miniemulsion Polymerization of Very Hydrophobic Monomers Initiated by a Completely Water-Insoluble Initiator: Thermodynamics, Kinetics, and Mechanism. *J. Polym. Sci. Part A Polym. Chem.*

2016, *54* (17), 2731–2745.

(54) Landfester, K.; Bechthold, N.; Tiarks, F.; Antonietti, M. Miniemulsion Polymerization with Cationic and Nonionic Surfactants : A Very Efficient Use of Surfactants for Heterophase Polymerization. *Macromolecules* **1999**, *32*, 2679–2683.

(55) Fedorov, A.; Liu, H. J.; Lo, H. K.; Copéret, C. Silica-Supported Cu Nanoparticle Catalysts for Alkyne Semihydrogenation: Effect of Ligands on Rates and Selectivity. *J. Am. Chem. Soc.* **2016**, *138* (50), 16502–16507.

(56) Cavin, L.; Rouge, A.; Meyer, T.; Renken, A. Kinetic Modeling of Free Radical Polymerization of Styrene Initiated by the Bifunctional Initiator 2 , 5-Dimethyl-2 , 5-Bis (2-Ethyl Hexanoyl Peroxy) Hexane. **2000**, *41*, 3925–3935.

(57) Shimizu, K.; Kamiya, Y.; Osaki, K.; Yoshida, H.; Satsuma, A. The Average Pd Oxidation State in Pd/SiO2 Quantified by L3-Edge XANES Analysis and Its Effects on Catalytic Activity for CO Oxidation. *Catal. Sci. Technol.* **2012**, *2* (4), 767.

(58) Alexeev, O. S.; Siani, A.; Lafaye, G.; Williams, C. T.; Ploehn, H. J.; Amiridis, M. D. EXAFS Characterization of Dendrimer - Pt Nanocomposites Used for the Preparation of Pt / γ -Al 2 O 3 Catalysts. *J. Phys. Chem. B* **2006**, *110*, 24903–24914.

(59) Hyde, T. I.; Ash, P. W.; Boyd, D. A.; Randlshofer, G.; Rothenbacher, K.; Sankar, G. X-Ray Absorption Spectroscopic Studies of Platinum Speciation in Fresh and Road Aged Light-Duty Diesel Vehicle Emission Control Catalysts. *Platin. Met. Rev.* **2011**, *55* (4), 233–245.

(60) Lei, Y.; Jelic, J.; Nitsche, L.; Meyer, R.; Miller, J. Effect of Particle Size and Adsorbates on the L3, L2 and L1 X-Ray Absorption Near Edge Structure of Supported Pt Nanoparticles. *Top. Catal.* **2011**, *54* (5), 334–348.

(61) Droll, H. A.; Block, B. P.; Fernelius, W. C. Studies on Coordination Compounds. XV. Formation Constants for Chloride and Acetylacetonate Complexes of Palladium(II). *J. Phys. Chem.* **1957**, *61* (7), 1000–1004.